Journal Pre-proof

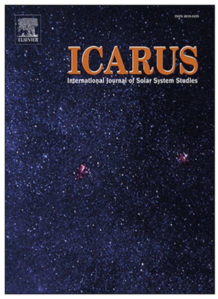

Gravitational re-accumulation as the origin of most contact binaries and other small body shapes

Adriano Campo Bagatin, Rafael A. Alemañ, Paula G. Benavidez, Manuel Pérez-Molina, Derek C. Richardson

PII: S0019-1035(19)30580-9
DOI: https://doi.org/10.1016/j.icarus.2019.113603
Reference: YICAR 113603

To appear in: *Icarus*

Received date : 8 August 2019
Revised date : 21 November 2019
Accepted date : 9 December 2019

Please cite this article as: A. Campo Bagatin, R.A. Alemañ, P.G. Benavidez et al., Gravitational re-accumulation as the origin of most contact binaries and other small body shapes. *Icarus* (2019), doi: https://doi.org/10.1016/j.icarus.2019.113603.

Gravitational Re-accumulation as the Origin of Most Contact Binaries and Other Small Body Shapes

Adriano Campo Bagatin, Rafael A. Alemañ, Paula G. Benavidez, Manuel Pérez-Molina

Departamento de Física, Ingeniería de Sistemas y Teoría de la Señal, Escuela Politécnica Superior, Universidad de Alicante, Spain

Instituto de Física Aplicada a las Ciencias y las Tecnologías, Universidad de Alicante, Spain

P.O. Box 99, 03080 Alicante (Spain). Phone: +34-965909943

Derek C. Richardson

Department of Astronomy, University of Maryland, College Park, MD20742, USA

Abstract

Asteroids show a variety of shapes, ranging from roundish to elongated to binary systems and contact binaries like (25143) Itokawa, the target of the Hayabusa mission (JAXA). These bodies spend most of their time within a collisional system, the asteroid belt, where impact processes are relatively frequent. Speculations on the origin of asteroid shapes invoke mechanisms such as collisions and spin-up effects. N-body numerical simulations of fragment evolution following catastrophic collisions have been recently carried out (Campo Bagatin *et al.*, 2018). In this study the idea that the stochastic process of gravitational re-accumulation may be responsible for many observed asteroid shapes is introduced. Asteroid contact binaries are shown to be regularly produced by the gravitational re-accumulation process following catastrophic impact. Similar processes may have occurred in the case of some comets and Trans–Neptunian Objects.

Keywords: Asteroids, Collisional physics, Contact binaries, Asteroid shapes

Email address: `acb@ua.es` (Adriano Campo Bagatin)

1. Introduction

Up to the late 1980s asteroids were detected only as small spots of light moving in the sky across the stars. At that time, the study of the dynamical parameters of their orbits and of their photometric colours were —together with light curves—almost the only available direct knowledge about them. That situation began to change dramatically with the first radar observations and especially since October 29th, 1991, when the *Galileo* probe took the first image of a main belt asteroid, *951 Gaspra*. It was the first time that we had the chance to see what an asteroid looks like, examine its shape and directly measure its size. Less than a dozen asteroids have been resolved by space probes and over one hundred–especially NEAs (Near Earth Asteroids)—have been observed by radiotelescopes since then, allowing the beginning of a new era in the study of asteroids. This has allowed improvement to the study of surface composition, morphology of craters, internal structure, rotation states, and shapes.

Speculations on the origin of asteroid shapes invoke mechanisms such as collisions and spin-up effects. The case of contact binaries is particularly interesting, that is elongated bodies in which two parts can be clearly identified: a body where most of the mass is, and a head, both resting on each other in a stable configuration. Tens of objects have been identified to be contact binaries by radar, spacecraft images and light curves, half of which were identified in the last 5 years. They include 6 comets, 10 TNOs (trans-neptunian objects) and almost 70 asteroids (http://johnstonsarchive.net/astro/index.html). In the case of NEAs, 12% are contact binaries according to radar detection statistics. Some simulations show unstable binary dynamics leading to contact binaries (Taylor & Margot , 2014), but Jacobson & Scheeres (2011) and Boldrin *et al.* (2016) showed that YORP spin-up may instead have led many NEA contact binaries to eventually evolve to binary systems or asteroid pairs. Regarding bilobated comets, Hirabayashi *et al.* (2016) identified a cyclic mechanism for fission and re-combination of comets, nevertheless not implying their origin.

Direct spacecraft images are available for four comets, one TNO and one asteroid, including comet 67P (Rosetta, ESA) and asteroid (25183) Itokawa (Hayabusa, JAXA). In addition, the New Horizons space probe recently revealed of TNO 2014 MU69 to be a contact binary with components of apparently roundish shape, but oblate. Dynamical mechanisms invoking non-gravitational effects like YORP (Rubincam, 2000) and BYORP (Steinberg

& Sari, 2011), acting on asteroid spins, have been proposed to explain the origin of contact binaries (Ćuk & Nesvorný, 2010). Such explanations may work in the case of some NEAs, due to their small size and proximity to the Sun, making YORP torque efficient. However, NEAs represent 70% of the observed contact binary sample, making a general explanation necessary to explain the morphology of any kind of small solar system bodies. In fact, the reason why some asteroids look roundish while others look elongated is not currently understood either, and no overall process responsible for such shapes has been identified to date. The fate of asteroid shaping is likely related to their collisional history and internal structure. Asteroids are formed inside the asteroid belt, where relative encounter speeds are distributed around 5.8 km/s and collisions are mostly catastrophic (Farinella *et al.*, 1992). Unfortunately, no direct measurement of asteroid interiors has been possible yet. Notwithstanding, experimental, theoretical, statistical, and numerical studies have been carried out over the last four decades and may help us to understand the processes that affect such bodies and may influence their structure and shape.

This study is part of a wide investigation about the process of fragment re-accumulation that follows high-speed impacts between asteroids. The detailed description of methodology of the overall study and quantitative results regarding asteroid density and porosity and their implications are in Campo Bagatin *et al.* (2018). Here we report about the results regarding morphology of asteroids and how different shapes are produced as a natural process in the gravitational re-accumulation of fragments.

2. Methodology

Most asteroids smaller than some 100 km in diameter are believed to be gravitational aggregates (Campo Bagatin *et al.*, 2001; Richardson *et al.*, 2002) formed in collisional processes in the main asteroid belt. **Many arguments support this assumption, from both obervational and theoretical, as summarized in Campo Bagatin *et al.* (2018).** For that reason, we perform numerical simulations of the collisional and dynamical evolution of irregularly shaped rigid fragments interacting under their mutual gravitational forces after a collision takes place. We briefly recall here the methodology followed in Campo Bagatin *et al.* (2018). Each rigid fragment (usually referred to as fragment or component) is modeled as a packing of tens to hundreds of rigid particles whose mutual distance is kept constant. Such fragments cannot deform nor break, so they move under rigid-body mechanical laws and can experience partially inelastic collisions with other fragments. Such simulations were performed using a soft-sphere discrete-element model N-body numerical code (PKDGRAV) (Richardson *et al.*, 2000; Stadel, 2001; Schwartz *et al.*, 2012). Re-acccumulation may happen right after a shattering collision of a coherent body or a previous gravitational aggregate has taken place. The overall idea is to concentrate our efforts on the phase in which some fragments have escaped the system and the remaining are beginning to re-accumulate. The shattering phase itself is out of the scope of our study (for more discussion, see Jutzi *et al.* (2015)) and our single fragments are not formed through clumping of smaller scale fragments, which is typical of former studies (e.g. Michel *et al.* (2004), Benavidez *et al.* (2018)). We draw the mass distribution of fragments, as well as their shapes, from results of laboratory shattering experiments carried out by Durda *et al.* (2015). Fragments are scaled and randomly placed in space with initial velocities and spins. In this way we build 36 rigid fragments, each made of tens to hundreds of spherical particles, with total $\sim$ 5000—10000 particles. The largest fragment of the distribution is placed in a central location, in analogy to what is observed in the outcome of laboratory experiments (as we show in Sec. 2.2). The initial conditions setup is repeated for each of the simulations, investigating the effect of different fragment mass density and total mass of the system. The mass distributions of fragments obtained in this way are in agreement with those describing post-fragmentation states of catastrophic disruption simulations by Jutzi *et al.* (2009, 2010). The final size of the aggregates range from $\sim$ 0.5 to $\sim$ 10 km. Simulations consist of allowing all fragments to gravitationally interact with each other and undergo mutual collisions. Each system eventually comes to rest in a permanent configuration with no further relative motion between components and with the overall spin corresponding to the angular momentum of the system, which ranges from low to high values and is conserved in the simulations.

2.1. Fragment mass distribution

The mass and shape distributions—in terms of aspect ratios—obtained in the laboratory experiments carried out at NASA Ames in 2015 (Durda *et al.*, 2015) were the starting point to build random distributions of masses and shapes of the synthetic components in numerical simulations. From each of the six collisional experiments at the NASA Ames Vertical Gun Range (AVGR), we worked out a relative mass (m_i/M) distribution and the aspect ratio for the largest 36 fragments obtained in shattering experiments (m_i is the mass of a generic fragment, M the mass of the target).

For any given simulation we run, we draw at random a number of fragments from the corresponding experimental distribution. We build our synthetic, irregularly shaped, components by extracting them from of a parent body that was obtained by randomly assembling a cloud of randomly distributed 5000 spherical particles that was allowed to collapse by gravitational re–accumulation. A suitable density is assigned to the whole parent body so that it will be the density of the extracted components. **This density corresponds to the meteorite analog density of the asteroid type to be simulated (e.g ρ =3.5 g/cm^3 for S-type and 2.5 g/cm^3 for C-type asteroids).** Each extracted component is a rigid aggregate made of spherical particles and it has a temptative 3D ellipsoidal shape whose axes ratios are randomly taken from the experimental distributions, as described in detail in Campo Bagatin *et al.* (2018). Specifically, for any given experimental fragment distribution, we draw at random mass ratios m_i/m_{LF} (m_{LF} is the mass of the largest fragment) from the corresponding experimental relative mass distribution and extract sets of aspect ratios from the values obtained from the empirical distributions of shapes. In this way we have—for each new generated component—a different set of axis ratios corresponding to each mass ratio. This procedure can be repeated as many times as needed depending on the number of components to be built. Finally the whole distribution is scaled to a convenient mass, keeping the density of components constant. Our nominal case is such that all components have an equivalent spherical diameter of ≈ 2 km altogether.

In any given simulation, components have to be located in space under suitable initial configurations. The largest component of the distribution is placed at the center of the coordinate system and the rest are randomly located in space freely or within a given limiting volume. Overlaps are avoided in the set up process by suitable random spacing. Different initial fragment distributions are shown in Fig. 6 and movies 1 to 3 (online supplementary material).

Different values for the limiting overall volume were considered to check the dependence of the results on initial conditions. We chose volumes in power of 2 relative to the aggregate volume (V_e). V_e is the volume of the equivalent sphere of the total mass of the components, assuming it has the same density of the components.

This choice corresponds to five different initial boundary spherical volumes to contain the created components. Volumes are set in such a way that they double with respect to each other: $V_4 = 2V_3 = 4V_2 = 8V_1 = 16V_e$, where V_e is the volume of the sphere equivalent to the aggregate volume.

The velocities of components are directed towards the center of mass and a spin vector is assigned randomly to each component within given ranges quantified below. The speed distribution is taken as uniform up to values smaller than the escape speed (typically a few tens of cm/s for km-size objects, depending on the mass of the system). In this way, initial conditions are a snapshot of the dynamical situation of the components that are bound gravitationally, once they have reversed the direction of their velocity vector and are on their way back to the center of mass of the system. The velocity distribution at that point is largely unknown for real re–accumulation processes. Also, fragments do not reverse their direction of velocity at the same time in real re–accumulation events. Therefore, assuming any kind of distribution at a given time is indeed arbitrary; for that reason we chose a simple uniform distribution of speed values. No mass-velocity dependence is assumed in this phase.

The rotation period of each component was also drawn from a flat distribution spin period, in the range 0-12 h. Again, there is little knowledge of the spin distribution of fragments resulting from shattering experiments, therefore any assumption is arbitrary. Main Belt asteroids are collisionally evolved, which causes their spin periods to approximately match a maxwellian distribution (Farinella *et al.*, 1981) averaged at about 6 h. In our case, the spin distribution resulting from of shattering events is not necessarily non-uniform, however it is certainly not collisionally evolved. Therefore, we assumed a simple flat distribution for the spin rate of components centerd on the average value of Main Belt asteroid spin rates. Once radial velocities and spins are set, it is possibile to change the value of the overall angular momentum to match specific situations.

Additional angular momentum can be injected in the system as a whole at the end of the fragment distribution set up. That was done in all simulations labelled as 'Stage 2' (Table 2 and 3) of the first part of the study (Campo Bagatin *et al.*, 2018).

In this way, we are simulating the inital conditions of a mass distribution of fragments with irregular shapes that are at the beginning of the re–accumulation phase following a catastophic disruption where the fragments with ejection speeds larger than the escape limit have already left the system. Many different initial conditions were created corresponding to each of the experimental mass and shape distributions so that 104 numerical simulations were run, 89 of which were successful in producing stable gravitational aggregates around 2 km in size (the rest had too large angular momentum to produce single aggregates). Another set of 40 simulations was run to extend the results to the 0.5–10 km asteroid size range and to check the effect of simulation parameters, as reported and discussed in Campo Bagatin *et al.* (2018).

PKDGRAV allows the system to gravitationally and collisionally evolve until stabilization. When the simulation is over, volume, density and porosity are calculated by a suitable algorithm developed for this purpose.

2.2. Location of largest component

The numerical simulations performed in the frame of this research share a common assumption: the largest fragment occupies a central position in the space distribution of components at the start of each simulation. This is based on experimental evidence as is illustrated in movies 4 and 5 (online supplementary material). Even if not often explicitly stated in the literature, nor even usually quantified, this was a common result in collisional laboratory experiments since the 1980s. However, it was difficult to assess at that time due to the lack of high–quality, high–speed cameras and suitable software. Pictures and video recording of hyper–velocity impact fragmentation experiments can now show this is a usual pattern. The experimental results of Durda *et al.* (2015), which have been taken as a starting point of this study, show this pattern again. Fig. 1 shows frames from three impact shattering experiments performed at NASA AVGR. The target (a & c) and the situation a few milliseconds after the collision (b & d) are shown for 2 different views with the shape and position of the unshattered target to show the relative position of the largest fragment resulting from shattering. It is evident that—in all cases—the largest fragment is the closest to the center of the original target, with low speed relative to the center of mass of the system (also see Table 1). The rest of the fragments are always ejected at larger speeds. If this experimental behavior can be assumed at asteroid scale, then the largest component of the initial distribution of the re–accumulation phase shall generally occupy a central position, which is not necessarily coincident with the center of mass of the system.

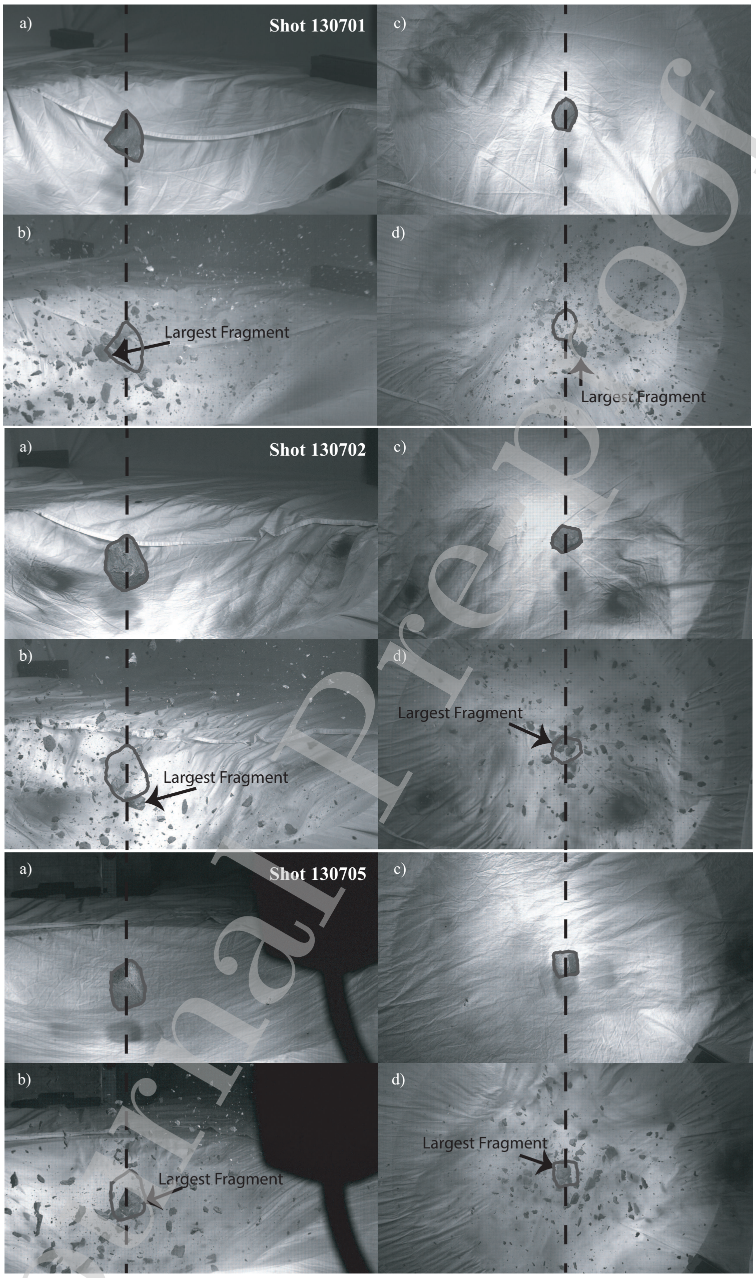

Figure 1: Snapshots of three shattering experiments. For each shot, side (a, b) and azimuthal (c, d) views show the position of the largest fragment 14, 24 and 20 ms respectively after the projectile impact. The original shape and position of the target are marked as a reference.

2.3. Mass distribution reliability

A comparison between the synthetic mass distributions obtained in our numerical simulations and published distributions of numerical simulations of asteroid shattering by SPH (Smoothed Particle Hydrodynamics) may be useful to assess the validity and compatibility of our results with different approaches to the problem. Jutzi *et al.* (2009) performed SPH numerical simulations of high-speed shattering of given targets and compared them to the laboratory results on targets with the same mass, material and the same impact speed. The size distributions obtained numerically were in reasonable agreement with the experimental ones. They showed that as a general trend their cumulative size distributions stay slightly below the corresponding curve for experimental results (their figures 3, 4, 5, 7, 9, 10, 11, 12, 13). For comparison, in Campo Bagatin *et al.* (2018), **figures 3, 4 and 5** show the cumulative mass distributions that we obtain in the generation of our fragments. The trend for those distributions is very similar to Jutzi *et al.* (2009): most stay slightly below the experimental curve. We can also compare the slopes of the experimental distributions in Durda *et al.* (2015)—which we use as a reference to build our synthetic distributions both in Campo Bagatin *et al.* (2018) and in this paper—and the size distributions obtained by former SPH fragmentation models, namely Jutzi *et al.* (2010). The latter reported cumulative size distributions with variable slope in two nominal cases in the $\alpha = (2.21, 2.24)$ range. This is in very good agreement with the slopes for the cumulative mass distribution reported in Durda *et al.* (2015), that were in the $\beta = (0.75, 0.82)$ range for two of the four experimental outcomes used. The relation between size and cumulative mass distribution slopes is $\alpha = 3\beta$, which allows a direct comparison between the two sets of distributions. In particular, the experimental cumulative mass distribution that was used to produce the numerical simulation that generates a contact binary similar to the shape of asteroid Itokawa is $\beta = 0.75$. In conclusion, we can state that the mass distributions used in our simulations—directly derived from experimental distributions—are in very good agreement with those found in shattering simulations, making our results compatible with the SPH approach shown in Jutzi *et al.* (2009, 2010).

3. Results

The final shapes of the end-state aggregate structures are generally irregular. Such structures typically take 3 to 5 hours to settle down. Different mass distributions, irregular fragment shapes and different angular momenta drive each system to particular configurations mainly driven by a stochastic process. Nevertheless, common patterns can be identified. Small initial separation between components favors formation of preservation of somewhat roundish configurations (81% of cases), as fragments can only travel a short distance before colliding with nearby components. These situations may correspond to relatively low-energy shattering collisions. In that case, the residual kinetic energy for fragments would be small allowing for small fragments displacement with respect to their original location in the parent body.

Contrary to what is commonly assumed to be natural for fragment reaccumulation, despite beginning at central location, the largest fragment ends up buried into the nucleus of the final aggregate only in 14% of our simulations. This is an unexpected result of our research and is fundamental in the explanation of the aggregate shapes as well as in the observation of asteroids and comets. The formation of relatively elongated objects with shapes very similar to the observed contact binaries is found in 23.6% of the simulations carried out, where two parts can be clearly identified as the head and the body of the object.

3.1. Shape classification

In order to analyze the results presented here we produce visual descriptions of the *pkdgrav* outcome. For any numerical simulation, each output corresponds to the time evolution of the physical quantities (size, mass, position, velocity, and spin vectors) of each of the 5000-10000 particles used, grouped into rigid aggregates at a given time step. Those are constructed into images that are eventually stitched into a movie using auxiliary code, including the public-domain ray-tracer POV-Ray. Different views are produced so that the qualitative morphologies of each end state can be suitably classified. Fig. 2 shows different aggregate morphology, ranging from rounded to elongated and contact binaries. Irregular shapes cannot be parameterized in a simple way, but still some rough classifications can be constructed, as follows.

The elongation parameter (Campo Bagatin *et al.*, 2018) is calculated from numerical output as a semi-quantitative measure of the separation of the largest component relative to the other fragments in each simulation. This is a measure of off-center mass distribution of the re–accumulated body and is calculated as the distance between the position of the center of mass of the largest component, $\vec{r}_{LC}$, and the position of the center of mass of the rest of components, $\vec{r}_{RC}$, normalized by the radius of the equivalent sphere of the aggregate (the sphere whose volume is equal to the volume of the aggregate itself), R_e.

$$E = \frac{|\vec{r}_{LC} - \vec{r}_{RC}|}{R_e}.$$

E discriminates between objects whose largest component occupies a central position (small $E > 0$ values) and those for which the largest component is away from the center. In this way it is possible to discriminate the separation of the largest component from the center of the distribution even in the case of roundish bodies. The stable gravitational aggregates obtained at the end of the 89 simulation were classified accordingly into the following classes:

- RC (Roundish-Centred): Morphologically roundish aggregates are characterized by low (< 0.4) values of the elongation parameter. That implies that the largest fragment is buried inside the aggregate, surrounded by smaller fragments. 14.6% of our simulations belong to that class.

- R (Roundish): Morphologically roundish aggregates characterized by values of the elongation parameter larger than in the RC case. That corresponds to largest fragments displaced with respect to the center during the re-accumulation process, showing up in the external part of the aggregate. These represent 28.1% of our simulations.

- E (Elongated): These aggregates have no roundish shape, fragments form a generically elongated object. The elongation parameter may be of no help in this case, as the largest fragment may occupy any position in the aggregate. However, most cases show an off-center position for the largest fragment. 25.8% of the cases show that morphology.

- CB (Contact-Binary): These shapes are analogous to some asteroid (or comet) contact binaries. That is, a main body formed by all the fragments but the largest, and a head (the largest fragment) in contact with one of the body ends. The elongation parameter typically takes large values for CB. 23.6% of our simulations end up that way.

- S (Satellite formation): When the shape of the gravitational aggregate is not very elongated, a fragment may have enough angular momentum to detach from the structure and orbit the main body. The stability of the satellite was not studied here. Only 3 simulations produced this result (3%).

- C (Clustered fragments): In some case, small aggregates of similar size form as independent bodies (not bound to each other). Mass ratios between any small aggregate and the main one were 0.5–0.2 (4.5% of simulations).

- L (Lost fragments): A few fragments (1 to 5) depart from the main formed aggregate at low speeds (a few tens of m/s to a few m/s) (4% of cases).

In summary, roundish shapes (class RC and R, 42.7%) and globally elongated (E and CB, 49.4%) are very common while satellite systems (3.4%) and similar-size clusters (4.5%) are seldom outcomes of our simulations. Loss of a few fragments happens in about half of the simulations generating E and CB morphologies. C and L cases may go on to be asteroid pairs or clusters, but this was not studied in detail. Morphological classes are not mutually exclusive, e.g., an L class may be in some case an E class for the main aggregate.

In Campo Bagatin *et al.* (2018) the Dynamically Equivalent Equal–Volume Ellipsoid (DEEVE) method was used to calculate the volume of our synthetic aggregates. This method identifies the triaxial ellipsoid whose volume is dynamically equivalent to that of the aggregate. A proof of this useful method is provided in the Appendix. We therefore derive the aspect ratio of our synthetic aggregates from the DEEVE (c/a and b/a, where a, b and c are the DEEVE axes, from largest to smallest) and compare them to those of the few asteroids and comets for which acceptable estimation of aspect ratios are available from spacecraft and radar observation. That includes mostly spacecraft visited and radar observed asteroids, a few observed comets and the only small TNO for which a close observation is available (New Horizons, NASA, on the 1^{st} of January, 2019). Fig. 3 shows how aspect ratios are distributed as compared to observed small bodies. Following Campo Bagatin *et al.* (2018), we consider two classes of simulated aggregates corresponding to two different density values of their components. They correspond to the two most common asteroid spectroscopic classes: S–type (high density, silicate composition) and C–type (low density, carbonaceous composition).

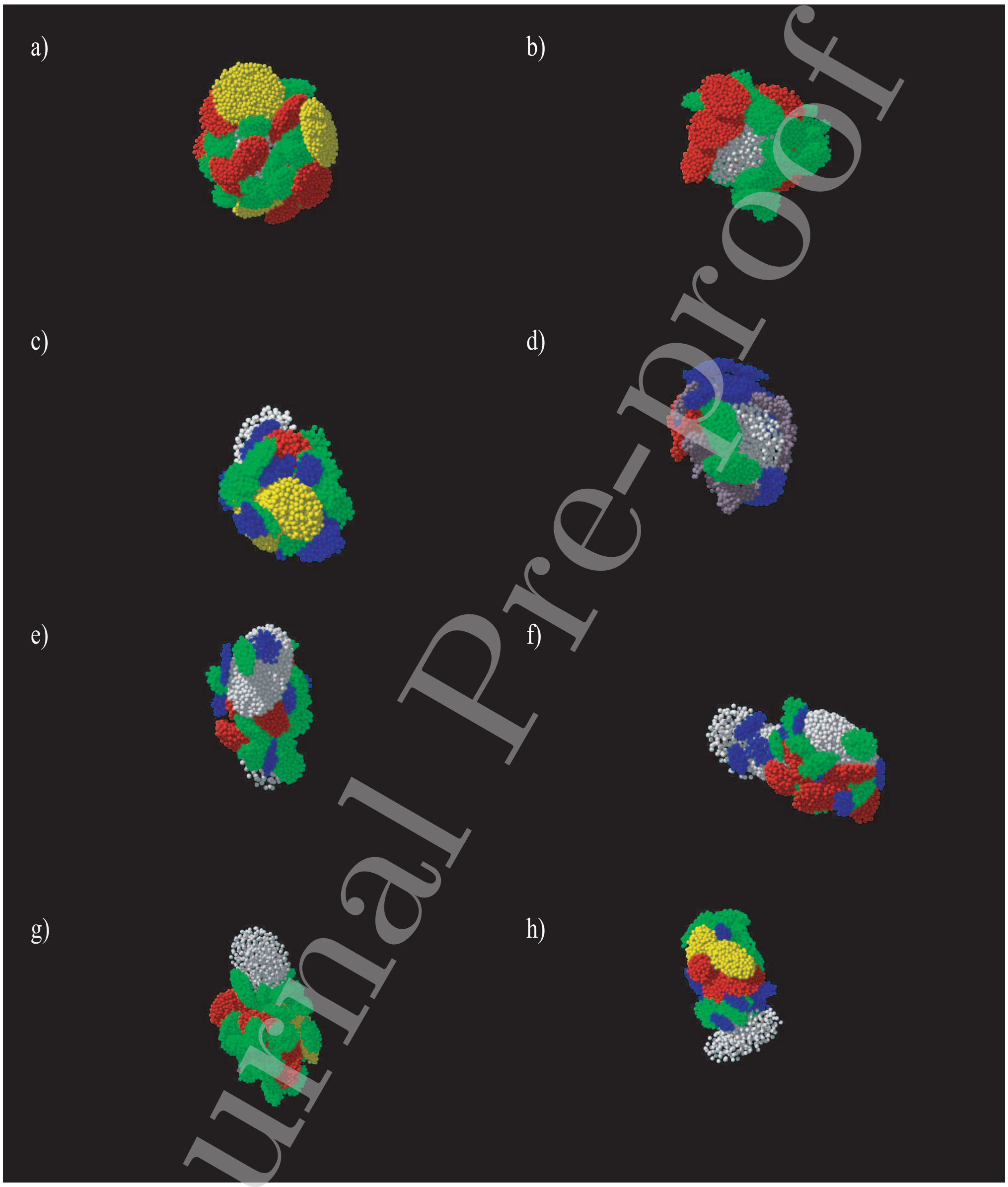

Figure 2: Snapshots of the end state of numerical simulations of 8 representative gravitational aggregates showing shape diversity. Different colors correspond to different masses of the discrete rigid aggregate components, as explained in Campo Bagatin *et al.* (2018).

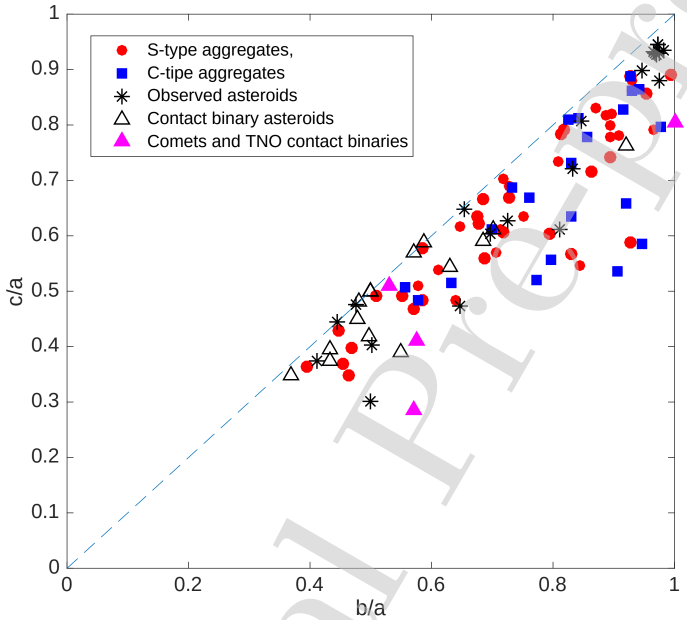

Figure 3: Aspect ratios c/a vs. b/a of the simulated aggregates. Full circles stand for S–type synthetic aggregates, full squares for C–types, according to the Campo Bagatin *et al.* (2018) classification. Asterisks stand for spacecraft and ground–based observed asteroids. Open triangles identify observed contact binary asteroids and full triangles observed comets and TNO 2014 MU69.

3.2. Dependence on initial conditions

Visual inspection of many simulated re-accumulation processes raises suspicion about the occurrence of roundish shapes being more frequent when the overall volume of the initial mass distribution is small, with few cases corresponding to elongated shapes. Therefore we checked the dependence of final aggregate shape on initial mass distibution in space. In order to do so, we calculated the component of the diagonalized inertia tensor—of both the initial and final distribution of mass—corresponding to the moment of inertia with respect to the shortest principal axis of inertia, in each case. That axis corresponds, in most cases, to the same direction of the angular momentum vector. In some cases the body is precessing about that axis so that those two directions are not necessarily coincident.

We compared the initial and final largest moments of inertia for all the simulated systems to check for dependence on initial mass distribution (Fig.4). In order to do so, we had to select only those simulations for which the mass of the bound system was conserved. As reported in Sec. 3.1, in some simulation a small number of fragments do not re–accumulate. It is necessary to have the same mass at the beginning and the end of each simulation in order to fairly compare initial and final space mass distributions. This selection preserves 52 simulations with equal final aggregate mass equal to the mass of the initial distribution. The initial largest moment of inertia, $(I_3)_0$, is normalized to MR^2 where M is the mass of the system and R is the radius of the DEEVE volume, $\bar{I}_0 = (I_3)_0/(MR^2)$. Such normalization implies that a sphere has a normalized value of the moment of inertia equal to 0.4. The moment of inertia of the final aggregate, $I_3 = m_e\left(a^2 + b^2\right)/5$, is instead suitably normalized to m_eR^2, where m_e is the mass resulting from the DEEVE calculation, $\bar{I} = I_3/(m_eR^2)$. In the Appendix we shortly show that the mass m_e is a dependent parameter in such calculation, that generally does not take the same value than the "real" mass M of the irregular aggregate itself. In fact, the DEEVE method finds the semi–axes of the ellipsoid with the same volume and the same principal moments of inertia of the irregular shaped aggregate and this requires that the value of the mass is derived accordingly to fit the DEEVE.

This analysis reveals that 2/3 of the simulations corresponding to $\bar{I}_0 < 10$ result in $\bar{I} < 0.5$, corresponding to roundish shapes. Instead, only 1/3 of simulations for which $\bar{I}_0 > 10$ result in $\bar{I} < 0.5$. This confirms a trend towards tight initial distributions preferring final roundish shapes, while less confined initial distributions give rise to any kind of final shape. In the latter case, the

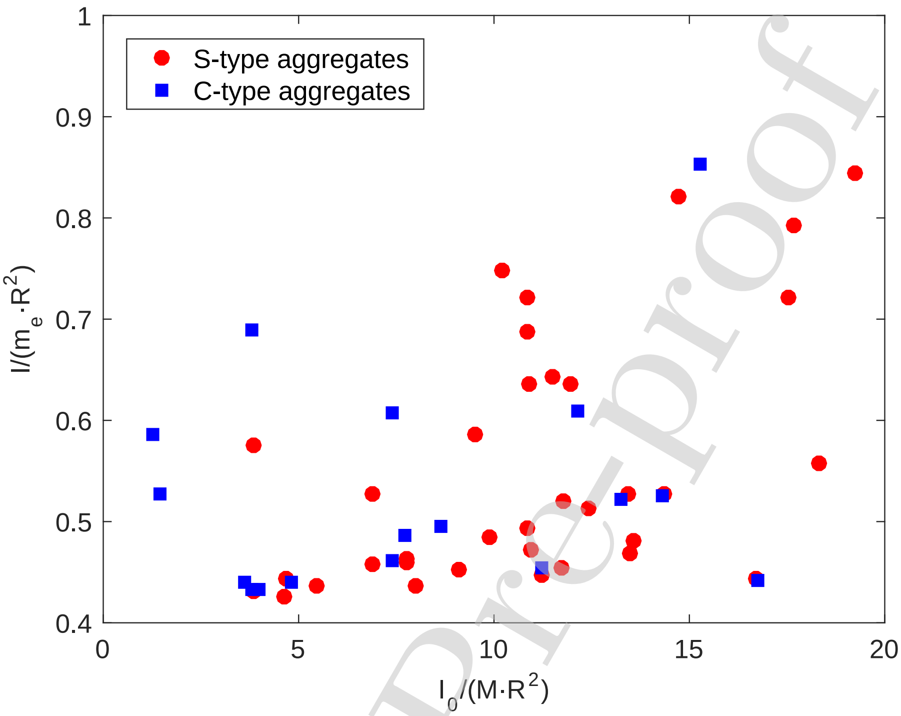

Figure 4: Normalized largest moment of inertia of initial (I_0) and final (I) mass distributions. As a reference, an exactly spherical distribution would give a value of the moment of inertia equal to 0.4.

re–accumulation process loses memory of the initial distribution, its evolution is dominated by hundreds of low–speed collisions between components with stochastic final configurations.

Fig. 5 shows no evidence of dependence of the final shape of aggregates—in terms of the largest moment of inertia, $\bar{I}$—on specific angular momentum values of the system, $< L >$, defined as

$$< L >= L/(GM^3R)^{1/2},$$

where M, R and L are, respectively, the mass, equivalent radius, and angular momentum of the object. The large amount of low–speed collisions between irregularly shaped components going on during the re-accumulation process seem to completely cancel the effect of initial angular momentum, at least for non–critical values ($< L_0 >> 0.015$. This range was not explored in detail in

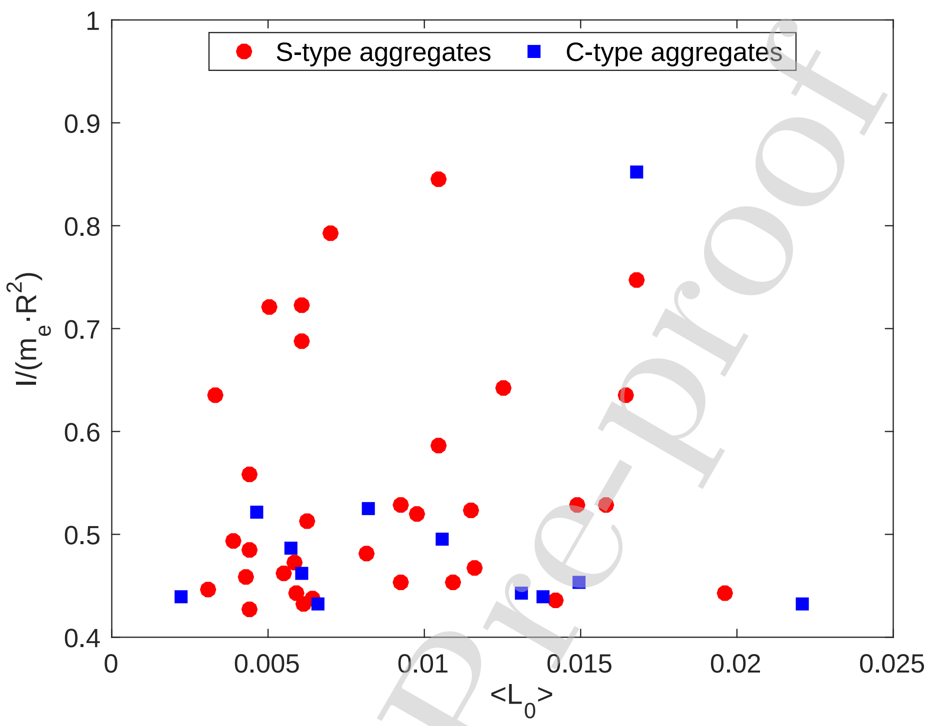

Figure 5: Normalized largest moment of inertia for final ($\bar{I}$) mass distributions corresponding to normalized values of normalized angular momentum, $< L_0 >$.

our investigation). This result is interesting as it implies that elongated asteroid shapes are not necessarily the result of initial high angular momentum configurations.

Further asteroid evolution due to spin-up or cratering collisions may change asteroid shapes and probably form "top" shapes, like in the case of the primary of many binary near—Earth asteroids and NEAs Ryugu and Bennu recently visited by the Hayabusa 2 (JAXA) and OSIRIS-REx (NASA) space missions. However, the explanation of evolved shapes is beyond the scope of the present work.

3.3. Benchmark Itokawa

We used a study carried out by Lowry *et al.* (2014) on the morphology and mass distribution of asteroid Itokawa as a benchmark for our own study. That group determined that the best fit to YORP measurements of Itokawa corresponds to a density ratio between the "body" and the "head" of 0.61 $\pm$ 0.14 and corresponding mass ratio of 0.21 $\pm$ 0.05. Mass ratios can be easily constructed by suitably setup of initial conditions in our simulations but density ratios depend on the mass distribution of fragments and their final arrangement. In our case, the comparison was done by calculating the average value of the ratios of the body density to the largest fragment density in the simulations that show contact binary structures. Our simulations have average density ratios of 0.57 $\pm$ 0.03, indicating a mass distribution of the body components quite in agreement with the estimate by Lowry *et al.* (2014) for Itokawa. The mass density of each part was determined using the following procedure. The head is removed from the output file containing the physical parameters of each particle of the whole body. The inertia tensor of the whole of the remaining fragments (the "body") is calculated and then diagonalized in order to set its principal axes of inertia along suitable reference system axes. At that point, the DEEVE can be employed to calculate the volume of the body and therefore its density is worked out (its mass is easily calculated as the sum of the masses of its particles). The same procedure is applied to the head. Finally the density ratios of the two parts are derived.

The average spin period for our synthetic CB types is 12.3 h, but the spin range spans a wide range from relatively fast (3.7 h) to slow (145 h) rotation; the median value is 10.3 hr. For comparison, asteroid Itokawas spin period is 12.1 hr. Specific angular momentum has an average value of 0.168 for our CB types. Values are quite dispersed so that the median (0.147) is a better estimate. For comparison, $< L >$ for asteroid Itokawa can be calculated as 0.158 from the Breiter *et al.* (2009) estimation of its moment of inertia and the Abe *et al.* (2006) and Fujiwara *et al.* (2006) estimations for the mass and size of the asteroid. Fig. 6 shows a comparison of the end state of a sample simulated contact binary morphology compared to asteroid Itokawa.

4. Discussion and conclusions

The visual analysis of the 89 movies corresponding to successful simulations reveals general patterns for the shaping of asteroid gravitational aggregates. We obtain many different shapes for gravitational aggregates, ranging from rounded to elongated and contact-binary. Contrary to what is generally imagined, only about 15% of simulated aggregates belong to RC class, that is roundish shape with the largest fragment in central position. R (roundish) bodies with the largest fragment located in non-central position

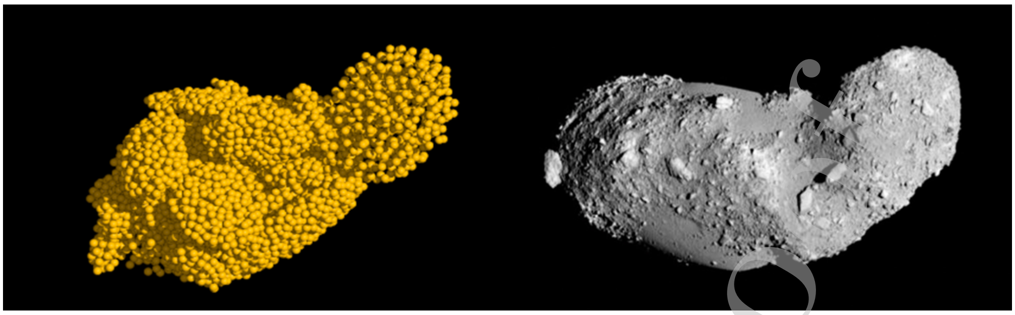

Figure 6: End state of contact binary (CB) morphology (left) compared to asteroid Itokawa as observed by the Hayabusa (JAXA) spacecraft (right). The largest fragment shows a slightly larger spacing between its spherical basic elements than the rest of fragments. This is due to the way in which the scaling from the synthetic largest fragment that matches laboratory experiments to km-size objects is made. However, the mass and overall size of the largest fragment is suitably scaled and the dynamics is not affected. Michel & Richardson (2013) show a similar numerical result for the morphology of asteroid Itokawa.

almost double (28%) RC class bodies. E (elongated) to CB (contact binary) aggregates are roughly half of the outocome of all our simulations, among them, a remarkable 24% belong to the latter class.

As a general conclusion, we suggest that the gravitational re–accumulation process is largely stochastic. It is dominated by low–speed multiple collisions between irregular fragments, generally loosing memory of initial conditions. We identified a general mechanism leading to elongated and—in particular—to contact–binary structure. In most simulations, at the beginning of the re–accumulation process, some component close to the largest fragment nudges it at low speed (tens of cm/s), forcing it slowly away from its central position, while the remaining fragments continue their fall towards the center of mass of the system (Fig. 7, movies 1 to 3: online supplementary material). Therefore, when re-accumulation is over (this process typically lasts 4 to 6 hours of real time), fragments are not clustered around the largest one, since it was removed from the center at the beginning. Instead, the largest fragment ends up at one end of the aggregate, for example as the "head" of a contact binary.

Our study is mainly focused on asteroids. Other populations of small bodies (comets that originate in the trans-Neptunian region or TNOs themselves) may not share a similarly intense collisional history. Therefore, extrapolation of the interpretation of results

for asteroids always has to be done with caution. Our results on the morphology of gravitational aggregates and contact binary formation are independent of fragment material density, as was expected; in fact no meaningful difference is found when density is changed from 3500 kg/m^3 to 2500 kg/m^3 (corresponding respectively to S-type and C-type asteroid meteorite analogues, as explained in Sec. 2). For this reason we suggest that similar process may take place in collisional events also in the trans–neptunian region, where most of the observed contact binary comets were likely generated. This genesis may be complementary to the mechanism proposed for the formation of comet 67P by Jutzi & Benz (2017) and in agreement with Schwartz *et al.* (2018), who also considered full collisional physics. In the trans–neptunian region—as in the asteroid belt—relative encounter speeds are currently in the catastrophic regime for the constituent materials (Dell'Oro *et al.*, 2013). Other comets, like Borrelly and Hartley 2, also show contact–binary shapes. Further debate on small body formation in the outer Solar System arose when TNO 2014 MU69 was observed by a fly-by of the New Horizons (NASA) space probe. 2014 MU69 is a 30 km size body formed by two clearly distinct components resting on each other. We can speculate that a re-accumulation origin of such body could be potentially possible by the mechanism described here. A collisional origin for such objects would need a relatively high impact rate at some point in the trans–Neptunian region, that cannot be presently ruled out. However, a close binary evolving to touching by some dissipative mechanism could also explain this object: a primordial origin for such a contact-binary structure (Jutzi *et al.*, 2015) would imply a soft collisonal evolution of individual components in a depopulated primordial environment.

It is also interesting to notice that binary systems arise spontaneously in a few simulations (e.g., movie 3 of the online supplementary material). For critical values of the angular momentum of the system, one of the fragments detaches from the spinning aggregate at the end of the re-accumulation stage and becomes a satellite around the central aggregate. Further evolution of the system was beyond the scope of this study.

Some NEA asteroid primaries and single bodies observed by radar and spacecraft observations show equatorial marks that can be suspected to be the former location of possible detached components (Tardivel et al., 2018). The described binary formation mechanism implies that our synthetic satellites are denser than the corresponding gravitational aggregate primaries. One of the very few estimates of density of both components of asteroid bi-

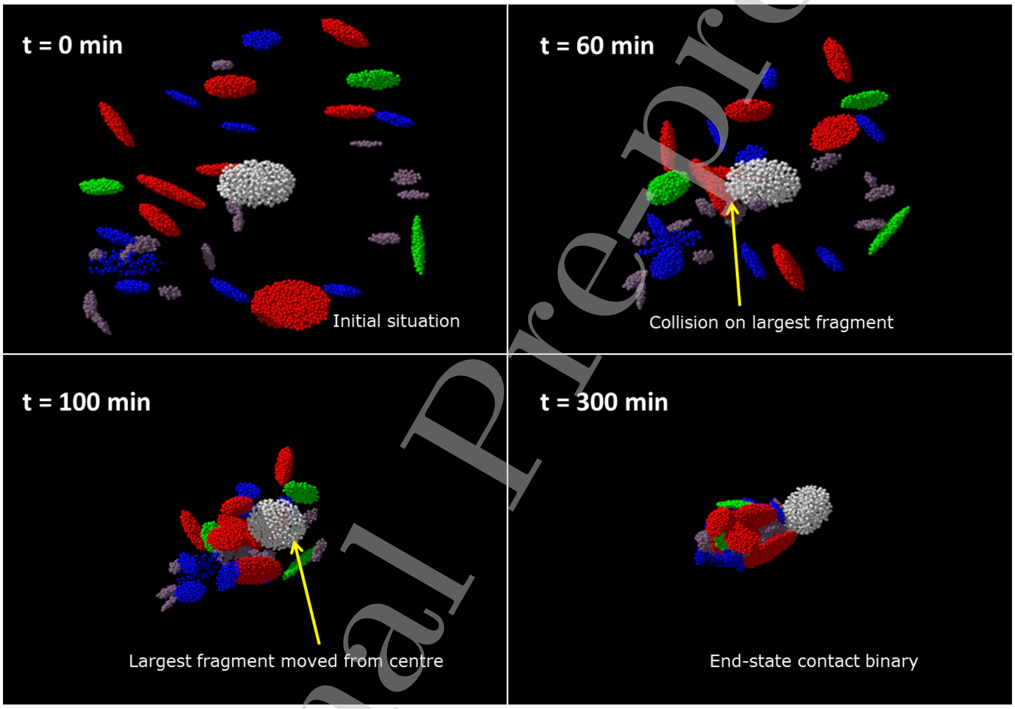

Figure 7: Schematic representation of the mechanism that drives the largest fragment away from its central position, leading to contact binary shape.

nary systems (1999 KW4) (Ostro *et al.*, 2006) indicates that the primary is in fact less dense than the satellite.

When angular momentum is larger than the critical value necessary for the formation of a satellite, loss of one or many components of the system occurs, with relative speeds on the order of several m/s in our simulations. The mass ratio of escaping components with respect to the rest of the body is in the 0.1 to 0.001 range, corresponding to the size ratios estimated for "asteroid pairs" and "asteroid clusters" (Pravec *et al.*, 2018). These are pairs and small groups of asteroids that have very similar orbital elements, whose orbits—once integrated back in time—lead to a common origin. Most of the clusters found by Pravec *et al.* (2018) can be explained by rotational fission due to spin up of the parent body. However, clusters (18777) Hobson and (22280) Mandragora are in the main belt and they likely need an alternative explanation for spin-up fission as the YORP effect is not viable in this case according to the authors. Our simulations suggest that a collision with injection of extra angular momentum to the system, followed by partial re–acccumulation of part of the parent body mass and the escape of fragments during the re–accumulation process may explain those systems. However, a dedicated study should be made to match the known characteristics of this those systems. It is worth reminding that formation of asteroid pairs and clusters is a different mechanism with respect to the formation of asteroid families: the discriminating parameter is the ejection speed of fragments. In the case of asteroid families, fragments are ejected at speeds far larger than the escape speed, typically on the order of hundreds of m/s. In the case of asteroid clusters, speeds are small, barely above the escape speed. Our simulations show that fragments initially bound escape eventually due to the excess of angular momentum of the system. The study of the size distribution, spins and speeds of the escaping fragments in our simulations is beyond the scope of this paper and shall be investigated in future work.

The process of gravitational re-accumulation of fragments following asteroid collisions offers a general mechanism to explain asteroid (and possibly comet) morphology, including contact binaries and some asteroid pairs and clusters, while it suggests a possible scenario for the formation of asteroid binary systems. Collisions were a key element during the formation and shaping of planetesimals in the primordial Solar System. Our results may contribute to the understanding of the early collisional processes that led to the building of the early rocky planets and the leftovers of that formation phase.

Acknowledgements

ACB and PGB acknowledge funding from AYA2016-79500-R (2016-2018) grant by the Spanish Ministerio de Economía, Industria y Competitividad.

References

Abe M., Takagi Y., Kitazato K., Abe S., Hiroi T., Vilas F., Clark B.E., Abell P.A., Lederer S.M., Jarvis K.S., Nimura T., Ueda Y., Fujiwara A. 2006. Near-infrared spectral results of asteroid Itokawa from the Hayabusa spacecraft. Science, 312(5778), 1334-1338.

Boldrin, L A. G., Scheeres, D. J., Winter, O. C. 2016. Dynamics of rotationally fissioned asteroids: non-planar case. Mom. Not. R. Astron. Soc. 461, 4 3982-3992.

Benavidez, P. G., Durda, D, D., Enke, B, L., Bottke, W, F., Nesvorn, D., Richardson, D. C., Asphaug, E., Merline, W. J., 2018. A comparison between rubble-pile and monolithic targets in impact simulations: Application to asteroid satellites and family size distributions. Icarus, 219, 1, 57-76.

Breiter, S., Bartczak, P., Czekaj, M., Oczujda, B., Vokrouhlick, D. 2009. The YORP effect on 25143 Itokawa. Astron. Astrophys. 507, 2, 1073-1081.

Campo Bagatin A., Petit J.-M., Farinella P. 2001. How many rubble piles are in the asteroid belt? Icarus, 149, 198-209.

Campo Bagatin, A., Alema, R. A., Benavidez, P. G., Richardson, D. C. 2018. Internal structure of asteroid gravitational aggregates. Icarus, 302, 343-359.

Ćuk, M., Nesvorn, D. 2010. Orbital evolution of small binary asteroids. Icarus 207, 2, 732-743 (2010).

DellOro, A., Campo Bagatin, A., Benavidez, P. G., Alema, R. A. 2013. Statistics of encounters in the trans—Neptunian region. Astron. Astrophys. 558, A95.

Durda D.D., Campo Bagatin A., Alemañ R.A., Flynn G.J., Strait M. M., Clayton A.N., Patmore E.B. 2015. The shapes of fragments from catastrophic disruption events: Effects of target shape and impact speed. Planet. & Space Sci. 107, 77-83.

Farinella, P., Paolicchi, P., & Zappala, V. 1981. Analysis of the spin rate distribution of asteroids. A&A, 104, 159.

Farinella, P., and D. R. Davis 1992. Collision rates and impact velocities in the main asteroid belt. Icarus 97, 111123.

Fujiwara, A., Kawaguchi, J., Yeomans, D. K., Abe, M., Mukai, T., Okada, T., Saito, J., Yano, H., Yoshikawa, M., Scheeres, D. J., Barnouin-Jha, O., Cheng, A. F., Demura, H., Gaskell, R. W., Hirata, N., Ikeda, H., Kominato, T., Miyamoto, H., Nakamura, A. M., Nakamura, R., Sasaki, S., Uesugi, K. 2006. The Rubble-Pile Asteroid Itokawa as Observed by Hayabusa. Science 312, 5778, 1330-1334.

Hirabayashi, M., Scheeres, D. J., Chesley, S. R., Marchi, S., McMahon, J. W., Steckloff, J., Mottola, S., Naidu, S. P., Bowling T. 2016. Fission and reconfiguration of bilobate comets as revealed by 67P/ChuryumovGerasimenko. Nature, 534, 352-255.

Jacobson, S. A., Scheeres, D. J. 2011. Dynamics of rotationally fissioned asteroids: Source of observed small asteroid systems. Icarus 214, 161-178.

Jutzi, M., Michel, P., Hiraoka, K., Nakamura, A., Benz, W. 2009. Numerical simulations of impacts involving porous bodies. II. Comparison with laboratory experiments. Icarus, 201, 802-813.

Jutzi, M., Michel, P., Benz, W., & Richardson, D. C. 2010. Fragment properties at the catastrophic disruption threshold: The effect of the parent bodys internal structure. Icarus, 207, 54.

Jutzi, M., Holsapple, K., Wnneman, K., Michel, P. 2015. Modeling asteroid collisions and impact processes. In: Asteroids IV. U.A.P., Tucson, 679-699.

Jutzi, M., Benz, W. 2017. Formation of bi-lobed shapes by sub-catastrophic collisions. A late origin of comet 67P's structure. Astron. Astrophys. 597, A62.

Lowry, S. C., Weissman, P. R., Duddy, S. R., Rozitis, B., Fitzsimmons, A., Green, S. F., Hicks, M. D., Snodgrass, C., Wolters, S. D., Chesley, S. R., Pittichov, J., van Oers, P. 2014. The internal structure of asteroid (25143) Itokawa as revealed by detection of YORP spin-up. Astron. Astrophys. 562, A48.

Michel P., Benz W., Richardson D.C., (2004). Catastrophic disruption of asteroids and family formation: A review of numerical simulations including both fragmentation and gravitational reaccumulations. Planetary & Space Science, 52, 1109-1117

Michel, P., & Richardson, D. C. 2013. Collision and gravitational reaccumulation: Possible formation mechanism of the asteroid Itokawa. Astron. Astrophys., 554, L1.

Ostro, S.. J., Margot, J.-L., Benner, L. A. M., Giorgini, J. D., Scheeres, D. J., Fahnestock, E. G., Broschart, S. B., Bellerose, J., Nolan, M. C. Magri, C., Pravec, P., Scheirich, P., Rose, R., Jurgens, R. F., De Jong, E. M., Suzuki, S. 2006 Radar Imaging of Binary Near-Earth Asteroid (66391) 1999 KW4. Science, 314, 5803, 1276-1280.

Pravec, P., Fatka, P., Vokrouhlick, D., Scheeres, D. J., Kunirk, P., Hornoch, K., Gald, A., Vratil, J., Pray, D. P., Krugly, Yu. N., Gaftonyuk, N. M., Inasaridze, R. Ya., Ayvazian, V. R., Kvaratskhelia, O. I., Zhuzhunadze, V. T., Husrik, M., Cooney, W. R., Gross, J., Terrell, D., Vilgi, J., Korno, L., Gajdo, ., Burkhonov, O., Ehgamberdiev, S. A., Donchev, Z., Borisov, G., Bonev, T., Rumyantsev, V. V., Molotov, I. E. 2018 Asteroid clusters similar to asteroid pairs. Icarus 304, 110-126.

Rubincam, D. P. 2000. Radiative Spin-up and Spin-down of Small Asteroids. Icarus 148, 2-11.

Richardson, D. C. , Quinn, T., Stadel, J. G., Lake, G. 2000. Direct large-scale N-body simulations of planetesimal dynamics. Icarus 143, 4559.

Richardson, D. C., Leinhardt, Z. M., Melosh, H. J., Bottke Jr., W. F., Asphaug, E. 2002. Gravitational aggregates: Evidence and evolution. In: Asteroids III. U.A.P., Tucson, 501-515.

Schwartz, S. R., Richardson, D. C., Michel, P. 2012. An implementation of the soft-sphere discrete element method in a high-performance parallel gravity tree-code. Granular Matter 14, 363380.

Schwartz, S. R., Michel, P., Jutzi, M., Marchi, S., Zhang, Y., Richardson, D. C. 2018. Catastrophic disruptions as the origin of bilobate comets. Nature Astronomy, 2, 379-382.

Stadel, J. G. 2001. Cosmological N-body simulations and their analysis. Thesis, University of Washington, Seattle. 126 pp.

Steinberg, E., Sari, R. 2011. Binary YORP and Evolution of Binary Asteroids. Earth and Planetary Astrophysics, 141, 2. 1, 11.

Taylor, P. A., Margot, J.-L. 2014. Tidal end states of binary asteroid systems with a nonspherical component. Icarus 229, 418-422.

Tardivel, S., Sánchez, P., & Scheeres, D. J. 2018. Equatorial cavities on asteroids, an evidence of fission events. Icarus, 304, 192.

Appendix: Dynamically Equivalent Equal Volume Ellipsoid (DEEVE)

Let B be a rigid body with principal moments of inertia I_1, I_2 and I_3 such that $I_1 \leq I_2 \leq I_3$, whose corresponding principal central axes coincide respectively with the axes X, Y and Z of a Cartesian frame $OXYZ$. The rigid body B has a mass M spanning over a region $\mathbb{V}$ with volume $V > 0$, so that, at each point of $\mathbb{V}$ with coordinates (x, y, z) in $OXYZ$, its volume mass density is $\rho(x, y, z) > 0$. With this notation we have that

$$I_1 = \iiint \rho(x, y, z) \left[y^2 + z^2\right] dxdydz,$$

$$I_2 = \iiint \rho(x, y, z) \left[x^2 + z^2\right] dxdydz$$

and

$$I_3 = \iiint \rho(x, y, z) \left[x^2 + y^2\right] dxdydz,$$

from which it readily follows that:

$$I_1 + I_2 - I_3 = 2 \iiint \rho(x, y, z)\, z^2 dxdydz \quad (1)$$

$$I_2 + I_3 - I_1 = 2 \iiint \rho(x, y, z)\, x^2 dxdydz \quad (2)$$

$$I_1 + I_3 - I_2 = 2 \iiint \rho(x, y, z)\, y^2 dxdydz \quad (3)$$

It is clear that $\rho(x, y, z)\, z^2 > 0$ for every (x, y, z) in the region formed by $\mathbb{V}$ excluding the plane $z = 0$, and the volume of such region is $V > 0$ (same as that of $\mathbb{V}$) because the plane $z = 0$ has a null volume[1]. This implies that $\rho(x, y, z)\, z^2$ is positive in a region of positive volume and null elsewhere, so the integral of Eq. 1 is strictly positive, thus being $I_1 + I_2 - I_3 > 0$. With analogous arguments for $\rho(x, y, z)\, x^2$ and $\rho(x, y, z)\, y^2$ the following relationships are obtained:

$$I_1 + I_2 - I_3 > 0, \quad I_2 + I_3 - I_1 > 0 \ \text{ and } \ I_1 + I_3 - I_2 > 0 \quad (4)$$

[1] From a mathematical viewpoint, the "volume" of a region is its Lebesgue measure in the space $\mathbb{R}^3$. In particular, the Lebesgue measure in $\mathbb{R}^3$ of any plane is zero.

The *Dynamically Equivalent Equal-Volume Ellipsoid* (DEEVE) of the rigid body B is a uniform ellipsoid that has the same volume V and the same principal moments of inertia I_1, I_2, I_3 as B. If m_e is the mass of the DEEVE and a, b, c are the semi–axes of the DEEVE contained in its principal central axes associated to I_1, I_2, I_3 respectively, then we have that:

$$I_1 = \frac{m_e}{5}\left(b^2 + c^2\right); \quad I_2 = \frac{m_e}{5}\left(a^2 + c^2\right); \quad I_3 = \frac{m_e}{5}\left(a^2 + b^2\right) \tag{5}$$

$$V = \frac{4\pi}{3}abc \tag{6}$$

From Eqs. 4 and 5 it readily follows that:

$$0 < I_2 + I_3 - I_1 = \frac{2m_e}{5}a^2 \tag{7}$$

$$0 < I_1 + I_3 - I_2 = \frac{2m_e}{5}b^2 \tag{8}$$

$$0 < I_1 + I_2 - I_3 = \frac{2m_e}{5}c^2 \tag{9}$$

By multiplying Eqs. 7 to 9:

$$\left(2m_e/5\right)^3 a^2b^2c^2 = \left(I_2 + I_3 - I_1\right)\left(I_1 + I_3 - I_2\right)\left(I_1 + I_2 - I_3\right) > 0,$$

which according to Eq. 6 leads to

$$\left(2m_e/5\right)^3 \left[3V/\left(4\pi\right)\right]^2 = \left(I_2 + I_3 - I_1\right)\left(I_1 + I_3 - I_2\right)\left(I_1 + I_2 - I_3\right) > 0.$$

Taking positive cubic roots[2] in the previous relationship it follows that

$$\left(2m_e/5\right) \cdot \left[3V/\left(4\pi\right)\right]^{\frac{2}{3}} = \left[\left(I_2 + I_3 - I_1\right)\left(I_1 + I_3 - I_2\right)\left(I_1 + I_2 - I_3\right)\right]^{\frac{1}{3}} > 0,$$

and thus:

$$m_e = \frac{5}{2}\left[\frac{4\pi}{3V}\right]^{\frac{2}{3}}\left[\left(I_2 + I_3 - I_1\right)\left(I_1 + I_3 - I_2\right)\left(I_1 + I_2 - I_3\right)\right]^{\frac{1}{3}} > 0, \tag{10}$$

whereas taking positive square roots in Eqs. 7-9 the following expressions for the semi–axes are obtained:

[2]Thus discarding conjugate-complex cubic roots without physical sense for m_e.

$$a = \sqrt{\frac{5\left(I_2 + I_3 - I_1\right)}{2m_e}} > 0 \tag{11}$$

$$b = \sqrt{\frac{5\left(I_1 + I_3 - I_2\right)}{2m_e}} > 0 \tag{12}$$

$$c = \sqrt{\frac{5\left(I_1 + I_2 - I_3\right)}{2m_e}} > 0 \tag{13}$$

Eqs. 10-13 provide the parameters m_e, a, b, and c of the DEEVE in terms of the parameters I_1, I_2, I_3 and V of the initially considered rigid body B.

It should be remarked that the condition $V > 0$ and its consequence given in Eq. 4 are necessary to avoid divisions by zero in Eqs. 10 to 13. Furthermore, the condition $I_1 \leq I_2 \leq I_3$ implies that[3] $I_2 + I_3 - I_1 \geq I_1 + I_3 - I_2 \geq I_1 + I_2 - I_3$, which—according to Eqs. 11 to 13—readily leads to $a \geq b \geq c$.

Notice that the DEEVE is the solution to the problem of finding a three–axial ellipsoid with semi–axes a, b, c, having the same principal moments of inertia and the same volume than those of some given body B (under the conditions specified above) with mass M. This leads to a rearrangement and suitable scaling of mass, that is now a parameter m_e which depends on V, I_1, I_2 and I_3, and is not—in general—coincident with the physical mass M of B. In fact, mass m_e has to be fit into the ellipsoid with the same volume V, so that the moments of inertia also coincide with the original ones. It is straightforward to check that for a parallelepiped P. Let P have a mass M and sizes h, k, l, such that its volume is $V = h \cdot k \cdot l$, Eq. 10 gives $m_e = \frac{5}{2}\left(\frac{4\pi}{3}\right)^{2/3}\frac{M}{6} \neq M$.

Therefore, when calculating the physical density ρ_B of a given body B, the expression $\rho_B = M/V$ has to be utilized.

[3]In fact $2\left(I_2 - I_1\right) \geq 0$ and $2\left(I_3 - I_2\right) \geq 0$, so $I_2 + I_3 - I_1 = I_1 + I_3 - I_2 + 2\left(I_2 - I_1\right) \geq I_1 + I_3 - I_2$ and in turn $I_1 + I_3 - I_2 = I_1 + I_2 - I_3 + 2\left(I_3 - I_2\right) \geq I_1 + I_2 - I_3$.

Shot	M (g)	m_p (g)	v (km/s)	$v_{rel_{LF}}$ (m/s)	$v_{rel_{per}}$ (m/s)
130701	433.0	0.1587	4.73	4.19	31.9
130702	534.6	0.1587	4.45	2.10	34.3
130705	479.1	0.1587	3.68	0.86	17.5

Table 1: Comparison of relative velocity of the largest fragment and a generic peripheral fragment, both relative to the center of mass of the system. The number of each experimental collisional shot—as in Durda *et al.* (2015)— is indicated in the first column. The mass of the target and the projectile and the impact speedare indicated in the second, third and fourth columns respectively. Relative velocity of the largest and that of a peripheral fragment, with respect to the center of mass, are indicated respectively in the fourth and fifth columns.

- Contact binary asteroids can be formed by gravitational re-accumulation.
- Rubble-pile asteroid shape formation is ruled by stochastic low speed collisions.
- Asteroid satellites formed during re-accumulation may be single shards.
- Largest fragments are not necessarily in the center of asteroid rubble-piles.